Engineering Structures 225 (2020) 111138

Contents lists available at ScienceDirect

Engineering Structures

journal homepage: www.elsevier.com/locate/engstruct

# Influence of cracking and rough surface properties on the transfer of forces in cracked concrete

Max Tirassa*, Miguel Fernández Ruiz, Aurelio Muttoni

*School of Architecture, Civil and Environmental Engineering, École Polytechnique Fédérale de Lausanne, Switzerland*

ARTICLE INFO

*Keywords:*
Concrete cracks
Shear transfer
Aggregate interlocking
Secondary cracking
Crack surface roughness
Mixed-mode fracture
Residual tensile strength
Mechanical modelling

ABSTRACT

Aggregate interlocking is acknowledged as one of the most significant actions transferring shear forces in cracked concrete structures and has been investigated for several decades. Despite the many experimental programmes and previous efforts to develop models based on mechanical approaches, a number of instrumental issues of the phenomenon are still not fully understood. For example, most researches have focused on the capacity to transfer forces through a given crack surface. However, the development of secondary cracks developing from the initial crack due to stress concentrations has traditionally been disregarded, despite the fact that these secondary cracks are governing in many cases for the overall strength. Also, other important aspects have not been comprehensively investigated, such as the contribution of the residual strength of concrete both in tension and shear during crack development. In this paper, the results of an experimental programme aimed at the fundamental understanding of the transfer of forces in cracked concrete is presented. This programme comprises detailed measurements of the surface roughness after failure. On that basis, a model considering both the crack surface properties and those of the concrete material is presented, accounting also for the potential development of secondary cracking. The model estimates the transferred forces by considering surface patches in contact and the contribution of the residual strength of the fracture process zone. The results of the model are compared to the test results showing consistent agreement both in terms of failure mode and the capacity to transfer forces as a function of crack opening and sliding.

## 1. Introduction

Concrete is a widely used construction material with high compressive strength but associated with a low strength and rather brittle response in tension. Reinforcement is normally arranged to control crack opening and to ensure a suitable transfer of tensile forces in a reliable manner. However, in many design situations, the structural resistance is controlled by the capacity of cracked concrete to transfer stresses without the assistance of any reinforcement. This is for instance the case of beams and slabs without transverse reinforcement subjected to shear. For these members, cracks typically develop in bending and propagate through the web leading to the development of a critical shear crack, potentially disturbing the theoretical compression strut carrying the load to the support (Fig. 1a) or other alternative load-carrying actions [4–6]. The kinematics of the critical shear crack (governing the local opening and sliding of crack lips) is associated with the location of the centre of rotation (R in Fig. 1b) near its tip [23]. At every point, the crack opens in the normal direction ($w$, see Fig. 1b, corresponding to Mode I opening, see also Fig. 2a) and can slide parallel to the crack direction ($\delta$, see Fig. 1b, corresponding to Mode II sliding, Fig. 2b). In general [4,5,7], the crack opens first in Mode I (as the centre of rotation is located near to the investigated point), but later progresses in Mixed-Mode I + II when the crack develops in a curved manner and the centre of rotation shifts its location (even originating a secondary crack from the flexural one, potentially becoming the critical shear crack [4], see Fig. 1c). Fig. 2c depicts a typical case following this kinematics, with an initial crack opening $w_0$ in Mode I followed by a Mixed-Mode opening with constant angle $\alpha$ (for symbols and notations refer to Table 1).

Due to the possible presence of a Mode II component and accounting for the rough nature of concrete crack surfaces, protruding material (typically aggregates) on one side of the crack can engage contact with the opposite side. This allows for a transfer of interface forces through the crack, a phenomenon commonly named as *aggregate interlocking*. These forces are considered to play a major role in the overall transfer of shear [5,28,35], and their calculation can be instrumental for estimating the shear resistance of beams [4–6]. Similarly to beams in shear, aggregate interlocking is also considered to

* Corresponding author.
*E-mail address:* max.tirassa@epfl.ch (M. Tirassa).

https://doi.org/10.1016/j.engstruct.2020.111138
Received 14 February 2020; Received in revised form 13 June 2020; Accepted 16 July 2020

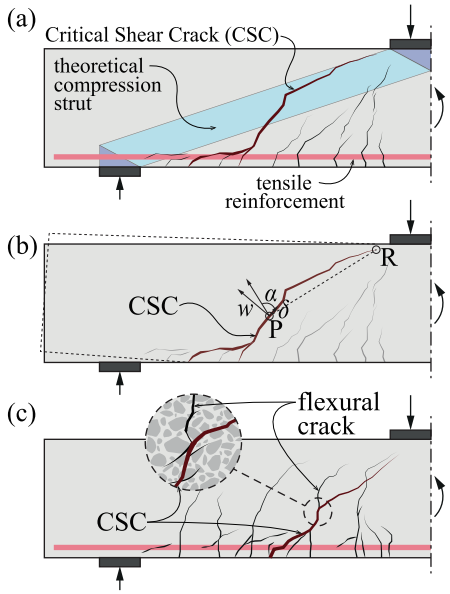


**Fig. 1.** Crack pattern and kinematics for a beam without transverse reinforcement failing in shear: (a) location of critical shear crack and theoretical strut carrying shear; (b) kinematics at a point of the critical shear crack; and (c) beam failing in shear due to development of secondary crack (adapted from [4]).

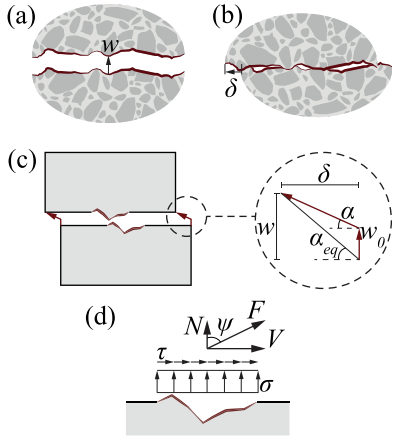


**Fig. 2.** Crack kinematics: (a) Mode I; (b) Mode II; (c) specimen subjected to Mode I followed by Mixed-Mode I + II; and (d) definition of positive stresses and internal forces.

potentially contribute to the transfer of forces in the case of punching of flat-slabs and footings [24], through rough construction interfaces [32] and has similarities with the shearing of rock surfaces [12].

### 1.1. Scales of roughness

Roughness of crack surfaces plays a major role in the capacity to transfer shear stress across the crack. For the purposes of this article, the following levels of roughness (similar to those introduced in [42]) will be defined:

- *Macro-roughness* is considered to be defined by the global crack geometry, which depends on the behaviour of a full-scale structure, as for example the shear crack shown in Fig. 1. These cracks are typically not straight, but bi-linear or curved [7], engaging different ratios of opening and sliding along their length.
- *Meso-roughness* is assumed to be related to the material constituents. The typical length to investigate the meso-roughness is comparable to the size of the maximum aggregates ($D_{max}$). Many testing programmes related to this scale can be found in [13,19,21,27,28,35,40].
- *Micro-roughness* is defined at the scale of the concrete matrix, with an associated length typically between 1/10 and 1/100 of $D_{max}$ [19,21]. It shall be noted that, due to the fractal nature of concrete surfaces [18], these patches are not planar, but also are rough surfaces.

**Table 1**
Symbols and notations

| Symbol | Description | Physical Dimension |
|---|---|---|
| $A_0$ | horiz. proj. of surface element | Area |
| $A_i$ | Area of surface element | Area |
| $D_{max}$ | Maximum aggregate size | Length |
| $G_F$ | Fracture energy | Force/area |
| $N$ | Force normal to crack plane | Force |
| $R_p$ | Roughness number (profile) | – |
| $R_s$ | Roughness number (surface) | – |
| $S$ | Soundness index | – |
| $V$ | Force tangential to crack plane | Force |
| $b$ | Specimen thickness, depth of crack plane | Length |
| $c$ | Width of crack plane | Length |
| $c_i$ | Constant value | – |
| $f_c$ | Concrete compressive resistance | Force/area |
| $f_{ct}$ | Concrete tensile resistance | Force/area |
| $l$ | length of segment | Length |
| $l_x$ | Length of horiz. proj. of segment | Length |
| $p$ | Segment penetration | Length |
| $u_M$ | Generalized Mixed-Mode opening | Length |
| $u_x$ | Displacement along horiz. $x$-axis | Length |
| $u_y$ | Displacement along vert. $y$-axis | Length |
| $w$ | Crack opening normal to crack plane | Length |
| $w_0$ | Initial Mode I crack opening | Length |
| $w_c$ | Crack opening without tensile strength | Length |
| $\alpha$ | Mixed-Mode opening angle (to crack plane) | Angle |
| $\alpha_{eq}$ | Overall opening angle (to crack plane) | Angle |
| $\gamma$ | Contact force angle to crack plane | Angle |
| $\delta$ | Crack sliding parallel to crack plane | Length |
| $\eta_c$ | Concrete strength factor | – |
| $\eta_{f_c}$ | Brittleness factor | – |
| $\eta_{conf}$ | Confinement factor | – |
| $\theta$ | Inclination of crack-profile segment | Angle |
| $\lambda_R$ | Factor for surface roughness | – |
| $\nu_\sigma$ | $\sigma$-activation due to FPZ interlocking | – |
| $\nu_\tau$ | $\tau$-activation due to FPZ interlocking | – |
| $\sigma$ | Stress normal to crack plane | Force/area |
| $\sigma_c$ | Contact stress | Force/area |
| $\tau$ | Stress parallel to crack plane | Force/area |
| $\psi$ | Angle to $x$-axis in $\sigma$-$\tau$ plot | Angle |
| 2PM | Two-Phase Model [40] | - |
| CSC | Critical Shear Crack | – |
| DIC | Digital Image Correlation | – |
| DSC | Dominant Secondary Crack/Cracking | – |
| DSC* | DSC starting from specimen's notch | – |
| NDSC | Non-Dominant Secondary Crack/Cracking | – |
| PC | Primary Crack/Cracking | – |

### 1.2. Experimental investigations

Test programmes on aggregate interlock have traditionally focused on concrete specimens pre-cracked by transverse splitting to induce a single (meso-scale) crack [21,39]. The transfer of forces associated with this crack is thereafter investigated under combined shear and normal forces [21,28,35,40]. In most cases, the dilatancy occurring when rough surfaces are subjected to Mode II kinematics is restraint by means of confinement normal to the crack plane. In early experiments, this confinement was provided with reinforcement which produced a constant normal force at yielding or by adapting the Mode I opening ($w$) at every load-step.

More recently, testing devices capable of applying loads in two directions and to control the crack kinematics have been developed

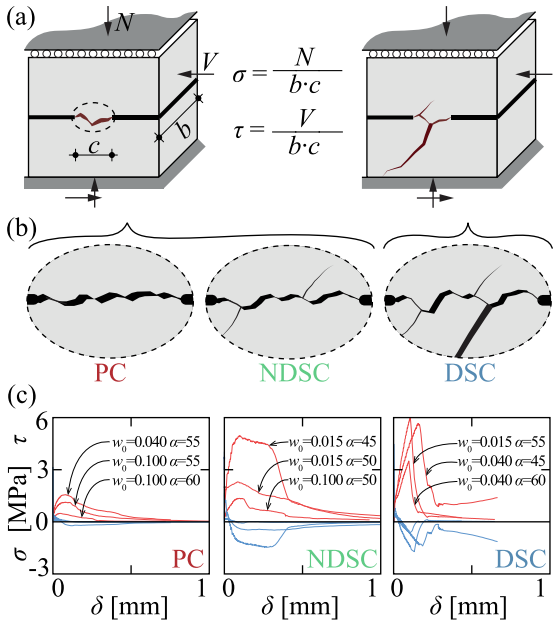


**Fig. 3.** Failure types due to aggregate-interlock engagement (see Section 2 for further information on the tests corresponding to the load–displacement curves): (a) meso-scale specimen and applied loads; (b) details of cracking area for various failure modes; and (c) load-sliding curves for tests with different failure modes (for definitions of $w_0$ and $\alpha$, see Fig. 2).

[13,27]. These more sophisticated testing equipments also allow pre-cracking the specimens in Mode I as a first load-step (rather than by transverse splitting before testing), and to control the kinematics accurately using multiple jacks in a closed-controlled loop [19]. Typical experimental results have allowed establishing a number of observations showing the influence of several parameters (as crack kinematics, level of crack opening, concrete strength and cracked surface properties) on the capacity to transfer shear forces. With respect to the development of cracking, a number of cases have been observed during experimental programmes reported in the literature. We can classify the different cases in three main categories described in the following.

1. Cracks initiate in Mode I [14] and, for this reason, specimens are often pre-cracked in tension before applying Mixed-Mode kinematics [19,27,39]. This first crack will be referred to in the following as the Primary Crack. Once this initial crack is subjected to kinematics with a Mode II component, shear and normal forces develop. When failure occurs by sliding of this crack, it will be named in the following as an aggregate interlock failure by *Primary Cracking* (PC), see Fig. 3b.
2. Often, local stress concentrations generate additional *secondary cracks* of varying size, which develop diagonally at an angle of approximately 45° from the primary crack and mostly open in Mode I [13,19,27]. Such cracks can remain stable and have limited influence on the overall behaviour, a case which will be named in the following as *Non-Dominant Secondary Cracking* (NDSC), see Fig. 3b.
3. Under some circumstances, the opening and growth of secondary cracks can progress, and, depending on the specimen geometry and its boundary conditions, this process can lead to a sudden failure [19,43] due to the uncontrolled development of a secondary crack. This latter case will be named as *Dominant Secondary Cracking* (DSC) in the following (see Fig. 3b).
   It shall be noted that in some tests of the literature, the dominant secondary crack develops not from the primary crack, but from a notch of the specimen. Such results are considered to be influenced by the boundary conditions and potentially not representative of the phenomenon itself. Such tests will be marked in the following as DSC*.

Different load–displacement curves and strengths are associated with the previously described cracking patterns and failure modes [37], as can be seen in Fig. 3c for some representative tests of the research programme presented later in this paper (see also Fig. 8b-e). For PC-tests, the shear forces increase gradually, reach a maximum value and eventually have a softening phase. Tests with NDSC have a similar response, but are typically subjected to higher scatter. Finally, DSC-tests tend to reach higher peak forces and are characterized by a sudden drop in the load when the secondary crack develops in an unstable manner (Fig. 3c).

In the literature, DSC-tests are often disregarded and considered as non-representative experiments, since most works focus on the response of the PC. However, investigations consistently report the development of secondary cracks at meso-scale [13,19,27,35] as well as at macro-scale in tests on structural members [4–6]. The practical significance of DSC is for instance shown in Fig. 1c, where a beam without stirrups failing by propagation of a critical shear crack is presented. According to the experimental measurements of Cavagnis et al. [4], such cracks can develop from a flexural one due to the local development of high contact stresses (associated with a large mechanical engagement between crack lips [4]). In addition, the development of DSC is consistent with the generation of secondary cracking in shear for members with transverse reinforcement. The development of such cracks (normally at flatter angles than flexural ones) is instrumental in so-called rotating crack models for the design of members with transverse reinforcement. These practical cases highlight the necessity of adopting general models for aggregate interlocking accounting for potential failures in DSC.

### 1.3. Theoretical approaches

With respect to aggregate interlock considered at the meso-scale, several models based on mechanical approaches can be found in the literature [2,3,8,19]. Two of the most representative ones are the Two-Phase Model by Walraven [39–41] and the Contact Density Model by Li and Maekawa [21], whose principles will be discussed in this paper, and whose implementation details are summarized in Appendix A and Appendix B.

### 1.4. Aims of the present work

Within this frame, this paper is aimed at addressing a number of open questions with respect to the transfer of forces by aggregate interlocking:

- Role of surface roughness on the transfer of forces via aggregate interlock
- Contribution of residual strength in fracture process zones to the transfer of shear and normal forces
- Development of different failure modes (PC, NDSC, DSC) as a function of roughness, material and kinematic parameters

This article presents the results of an experimental programme performed using a test set-up capable of pre-cracking double-notched concrete specimens in tension and then applying a given Mixed-Mode kinematics. Various types of concrete were investigated as well as different crack kinematics (with varying initial crack openings and opening-to-sliding ratios). Special attention is paid to the final crack surfaces, which were measured using a digital microscope. The results are eventually used to derive a model for the transfer of forces, taking into account the varying surface roughness of the primary crack and the material residual resistance in the fracture process zone.

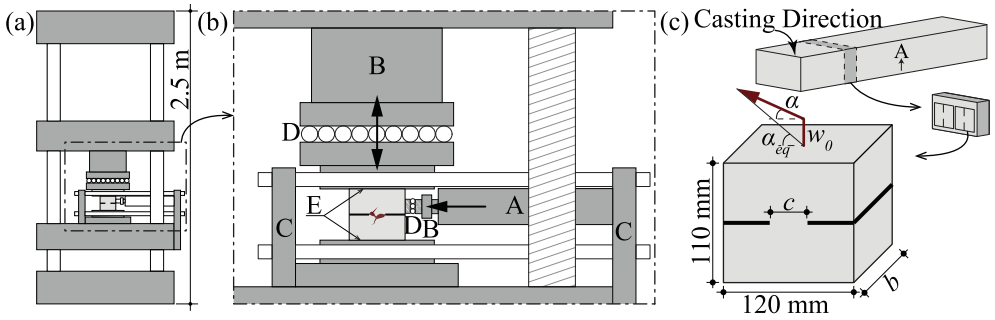


**Fig. 4.** Test set-up: (a) front view; (b) detail of front-view: A-horizontal jack; B-load cells; C-steel holding plates; D-sliding roller guides; E-glueing planes; and (c) production process, typical specimen and applied kinematics.

## 2. Experimental programme

### 2.1. Test set-up

The test set-up consisted of a high-precision Zwick electro-mechanical machine (acting in vertical direction) modified by addition of a hydraulic jack in the horizontal direction to apply displacements in two perpendicular directions on double-notched concrete specimens (Fig. 4). The specimens were glued on steel plates as shown in Fig. 4b. Following this procedure, it was possible to pre-crack the specimens up to an initial crack opening $w_0$ by performing a Mode I tension test in the vertical direction. Once the selected crack opening was reached, the initial Mode I phase ended and the specimens were subjected to Mixed-Mode with an imposed angle $\alpha = \arctan(\Delta w/\Delta\delta)$. To that aim, the horizontal jack applied shear displacements which resulted in sliding $\delta$ at the crack interface, while the vertical jack allowed additional increases of $w$ to follow the desired kinematics. During testing, the lower specimen half was fixed, while the upper part could move thanks to low-friction linear roller guides.

The crack opening and sliding were measured using a custom-made arrangement consisting of strain gauges calibrated using LVDTs for that purpose. Such device allowed for independent measurements of vertical and horizontal displacements. The displacement-control device is further described in [37]. The initial displacement rate of 0.1 μm/s was selected so that for a typical test resulting in PC, the initial Mode I part lasted 5–15 min depending on the value of $w_0$ (tensile strength was reached after about five minutes), while the Mixed-Mode phase lasted about an hour to reach the maximum shear force. After the peak was reached, the displacement rate was progressively increased until the test finished when the forces were very low or the maximum stroke was reached (approximately 3 mm). Apart from the recordings from the load cells and the displacement-measuring devices, most tests were additionally monitored using Digital Image Correlation.

### 2.2. Specimens

The test specimens were produced from several concrete prismatic specimens that were cast and cured under sealed conditions for at least 28 days. They were then demoulded and cut into slices of thickness $b$ (nominal thickness equal to 50 mm) using a circular saw (see process in Fig. 4c). Two specimens with notches of varying length were obtained from each slice with a water-jet cutting machine. The orientation of the specimens was selected in order to minimize the influence of the casting direction (Mode I pre-cracking direction was perpendicular to the casting direction, thus reducing the influence on the tensile strength of weak interfacial transition zones between aggregates and cement matrix due to bleeding [10,16]). The final shape of the specimens is shown in Fig. 4c, where the width of the crack plane between the notches is indicated as parameter $c$. Three different concrete castings were prepared with the mix designs reported in Table 2. The granulometric curves for the different mixes are additionally presented in Fig. 5. The exact geometry of the specimens and compressive strength of concrete at the day of testing ($f_c$) is reported in Table 3, where the first two digits of the specimen numbers indicate the corresponding casting batch.

### 2.3. Test results

Fig. 6 presents a summary of the maximum measured strengths as a function of the angle at failure accounting for the initial crack opening ($\alpha_{eq}$, see Fig. 4c). This figure also includes tests from the literature for comparison purposes [19]. Further details of the specimens are given in Table 3 and the complete shear and normal curves recorded for all specimens are reported in Appendix C.

As shown in Fig. 6, tests develop higher forces for kinematics with a larger Mode II component (corresponding to values of $\alpha_{eq} < 60°$). The tests of current research tend to fail in DSC or NDSC while for higher values ($\alpha_{eq} > 65°$), PC was dominating. Although the applied kinematics influence the failure mode, they are insufficient to entirely explain it. As discussed in the following section, the surface roughness of the initial crack and its distribution represent additional instrumental parameters governing the crack development. Nevertheless, the use of $\alpha_{eq}$ as a parameter results in a clear trend even though the initial crack opening $w_0$ can vary significantly. Moreover, it can be seen that tests with PC and NDSC behave similarly, while specimens with DSC diverge significantly from them and are associated with higher interlocking forces.

An aspect extensively discussed by previous researchers is the relationship between the tangential and the normal force developing under given kinematics [21,39], expressed using the angle $\psi$ hereafter ($\tan\psi = \tau/|\sigma|$, see Fig. 2d). Fig. 7a illustrates a typical response for this parameter. The plot shows the measured values of $\tau$ and $\sigma$ and the corresponding values of $\psi$ as a function of the recorded sliding $\delta$. It can be noted that after the initial Mode I phase ($\delta = 0$, Fig. 7b), some residual tensile strength is still present between the notches, resulting in values $\sigma > 0$. At this moment, shear displacements are applied ($\delta > 0$), leading to an active engagement of the cracked surfaces. This results in a rapid increase in the shear stress $\tau$ but also in the development of additional compressive normal stresses ($\sigma$) related to aggregate interlocking to avoid crack dilatation above the limits set by the kinematics (angle $\alpha$). The value $\psi_{max}$ is reached consequently when $\sigma$ becomes zero (Fig. 7c). Thereafter, both $\tau$ and $|\sigma|$ continue to increase (Fig. 7d), but the normal forces tend to become more significant as the sliding increases (resulting into progressively decreasing values of $\psi$). This behaviour occurred for all tests, showing the significance of crack dilatation and of the associated normal forces. As a result, the rate of decrease in $\psi$ after its peak value depends on the externally applied kinematics, with lower values of $\alpha_{eq}$ (associated with higher values of $\sigma$) leading to lower values of $\psi$. This trend can be observed in Fig. 8, where the values of $\psi$ are reported at the instant $\tau_{max}$ for all tests as a function of the applied kinematics. This response is in addition confirmed by the results of pure Mode II tests (performed by Li et al. [21]) corresponding to low values of $\alpha_{eq}$ and resulting in values $\tau \approx \sigma$ ($\psi$ close to 45°).

**Table 2**
Mix designs for the concrete castings.

| | Casting # | | |
|---|---|---|---|
| | 02 & 03 | 04 & 05 | 07 |
| $D_{max}$ [mm] | 16 | 8 | 8 |
| Water [kg/m$^3$] | 172 | 204 | 177 |
| Cement [kg/m$^3$] | 310 | 316 | 321 |
| Cement Type | CEMII A-LL42.5R | CEMII A-LL42.5 N (white) | CEMII A-LL 42.5 N |
| Aggregates [kg/m$^3$] | 1955 | 1809 | 1853 |
| Petrography of aggregates | Hard gravel, Rhone valley, Riddes (CH), limestone, granitoids, sandstone, quartzite | Medium-Hard gravel, Quarry in Villeneuve (CH), ~95% limestone | Medium-Hard gravel, Pit in Savigny (CH), ~85% limestone |
| $f_{c,28}$ [MPa] | 32.8–30.6 | 29.8–25.7–24.7 | 30.1–37.1–28.9 |

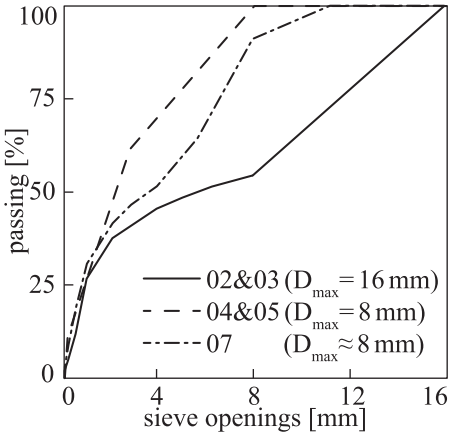


**Fig. 5.** Granulometric curves for the concrete castings.

**Table 3**
Dimensions of tested specimens, crack kinematics, compressive concrete strength and failure mode (the first two digits of the specimen number indicate the casting, the middle digits the slice number, see Table 2 for $D_{max}$ and other information; PC: failure by primary cracking; NDSC: failure with non-dominant secondary cracking; DSC: failure by dominant secondary cracking starting at primary crack; DSC*: failure by secondary cracking originating at notches)

| # | $b$ [mm] | $c$ [mm] | $w_0$ [mm] | $\alpha$ [°] | $f_c$ [MPa] | Failure |
|---|---|---|---|---|---|---|
| 021501 | 51 | 18.0 | 0.040 | 40 | 38 | DSC* |
| 021601 | 51 | 19.0 | 0.025 | 45 | 38 | NDSC |
| 022002 | 51 | 19.0 | 0.015 | 45 | 38 | NDSC |
| 022101 | 51 | 19.0 | 0.100 | 40 | 39 | DSC |
| 022102 | 51 | 24.0 | 0.040 | 45 | 39 | NDSC |
| 030101 | 52 | 26.5 | 0.100 | 60 | 39 | DSC |
| 030201 | 51 | 20.5 | 0.040 | 45 | 39 | DSC |
| 030802 | 51 | 23.5 | 0.100 | 55 | 39 | PC |
| 030901 | 50 | 25.0 | 0.100 | 60 | 39 | PC |
| 040501 | 50 | 24.0 | 0.015 | 50 | 29 | NDSC |
| 040601 | 51 | 33.5 | 0.020 | 50 | 29 | NDSC |
| 050101 | 50 | 23.5 | 0.100 | 45 | 32 | DSC |
| 050102 | 50 | 18.5 | 0.025 | 50 | 32 | NDSC |
| 050202 | 50 | 18.5 | 0.015 | 45 | 32 | DSC* |
| 050301 | 51 | 23.5 | 0.040 | 55 | 32 | PC |
| 050302 | 51 | 19.0 | 0.025 | 45 | 32 | NDSC |
| 050401 | 50 | 22.5 | 0.040 | 50 | 32 | NDSC |
| 050801 | 51 | 23.5 | 0.100 | 50 | 32 | NDSC |
| 050802 | 51 | 18.5 | 0.015 | 55 | 32 | DSC |
| 050902 | 51 | 18.5 | 0.015 | 50 | 32 | NDSC |
| 070101 | 52 | 18.5 | 0.040 | 60 | 47 | PC |
| 070302 | 50 | 19.0 | 0.015 | 55 | 47 | DSC |
| 070501 | 51 | 26.5 | 0.040 | 60 | 47 | DSC |
| 070601 | 50 | 24.0 | 0.100 | 50 | 47 | NDSC |
| 070902 | 50 | 17.0 | 0.015 | 55 | 48 | PC |
| 071401 | 51 | 19.5 | 0.015 | 50 | 48 | PC |

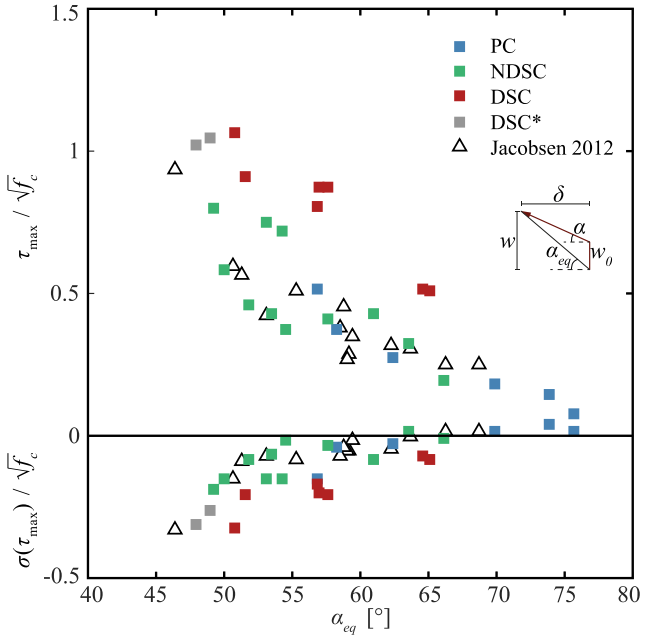


**Fig. 6.** Peak values at instant $\tau = \tau_{max}$ as a function of $\alpha_{eq}$(=arctan($w(\tau_{max})/\delta(\tau_{max})$)) (including tests from [19]).

### 2.4. Surface roughness

As previously highlighted by a number of studies [19,21], the crack geometry and the crack surface are important parameters governing the forces transferred through aggregate interlocking. For the present investigation, the specimen surfaces were scanned after failure using a Keyence VHX 5000 digital microscope with VH-Z100R lens at 100X magnification. This allowed for the detailed recording of the surface geometry, with a data-point approximately every 2 μm (Fig. 9b). The surface was approximated as a series of profiles defined as parallel to the shearing direction (Fig. 9c). These sections were spaced 1 mm from each other in the $y$-direction, while the $x$-coordinate was assigned every 0.1 mm. For each point, the corresponding $z$-coordinate was calculated as the average value in a zone of size $\Delta_x$ and $\Delta_y$, both equal to 0.1 mm (Fig. 9d-e). The inclination $\theta$ of each micro-segment with respect to the horizontal was calculated on this basis. The roughness of the crack surfaces at the considered scale can be characterized in several manners:

1. The relative distribution of profile-segments as a function of their steepness $\sum_{\Delta\theta} l / \sum l_x$, where $\Delta\theta$ specifies the considered interval of angles. The average relative occurrence of segments inclined within intervals of $\Delta\theta = 10°$ is reported in Fig. 10. It can be noted that surfaces corresponding to DSC have a higher percentage of steep

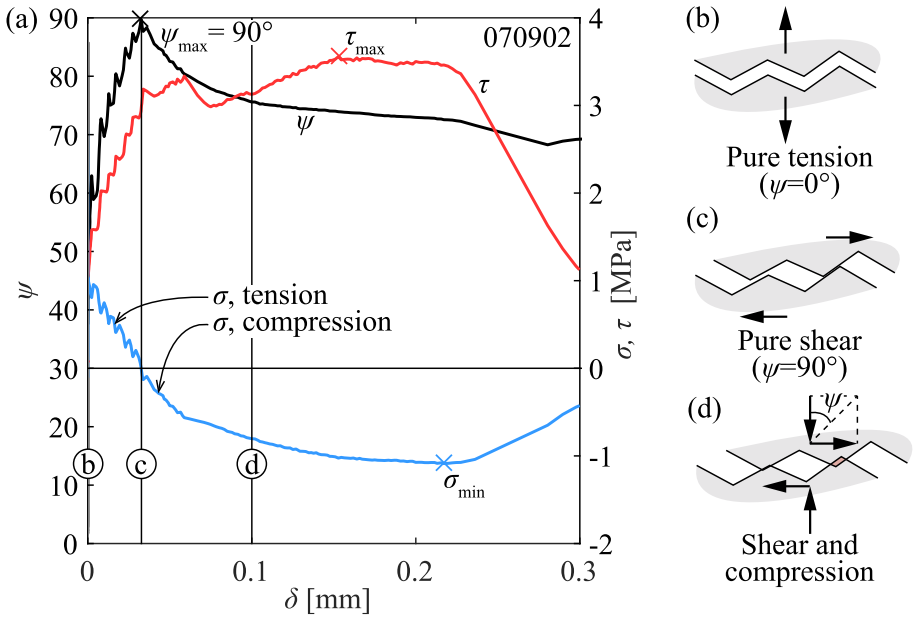


**Fig. 7.** Activation of interlocking forces for test 070902: (a) evolution of $\psi$; (b) forces acting on crack after Mode I phase; (c) progressive activation of $\tau$, while $\sigma$ goes to zero; and (d) increasing normal forces to control crack dilatation.

segments in the range $50° < \theta < 90°$. As shown in Fig. 10b, such segments are the most likely to engage contact for the kinematic ranges investigated in this research ($40° < \alpha < 60°$). Differently, segments with negative or rather small values of $\theta$ (Fig. 10c-d) are less likely to engage in contact with the opposite crack side. With respect to surfaces of tests resulting in NDSC and PC, they are observed to have relatively few steep segments, which explains why they result in weaker forces and limited secondary crack propagation.

2. The profile roughness index $R_p$ (called $A_t$ in [21]), defined as:

$$R_p = \frac{\sum l}{\sum l_x} \tag{1}$$

where $l$ is the length of a segment and $l_x$ its projection with respect to the horizontal (Fig. 9e). Values $R_p$ close to 1.00 indicate rather flat cracks while higher values of $R_p$ (recorded up to approximately 1.30) indicate rougher surfaces. The calculated values are reported in Table 4.

3. Similarly to $R_p$, the surface roughness index $R_s$ compares the horizontal projection of the crack surface $\Sigma A_0$ with the crack surface $\Sigma A_i$ (Fig. 12b):

$$R_s = \frac{\Sigma A_i}{\Sigma A_0} \tag{2}$$

The term $\Sigma A_i$ is calculated by considering the surface as a grid of data points identifying a series of triangles whose areas are summed. The roughness area index depends on the selected grid spacing and increases for smaller spacings [20]. To allow for a reliable comparison of the measured values, several authors set the distance between two data-points as equal to 0.25 mm [17,29]. In [17], the following relation between compressive strength and $R_s$ was

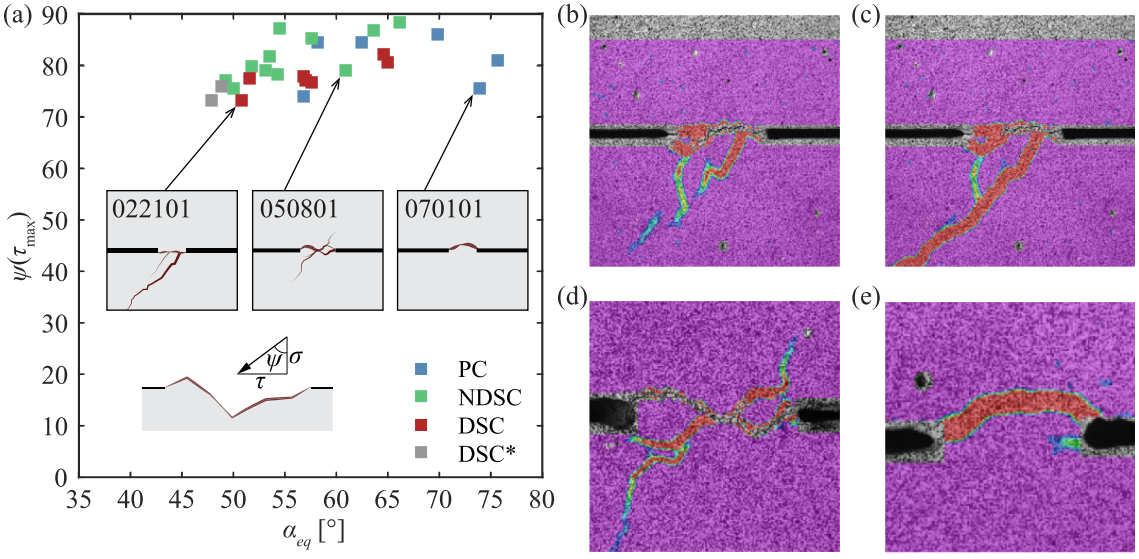


**Fig. 8.** (a) Value of $\psi$ at $\tau = \tau_{max}$ for all tests; (b) DIC-image for test 022101 (DSC) shortly prior to peak shear stress; (c) DIC-image for test 022101 after peak and propagation of secondary crack; (d) DIC-image for test 050801 (NDSC) at peak shear stress; and (e) DIC-image for test 070101 (PC) at peak shear stress (for tests with NDSC and PC the cracking pattern did not change significantly after the peak).

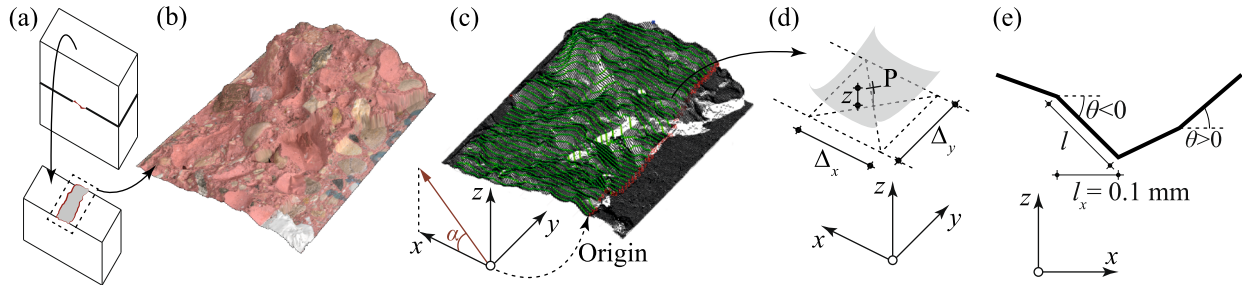


**Fig. 9.** Example of crack surface (specimen 070501): (a) Scan of upper half of tested specimen; (b) Scanned surface; (c) Extraction of profiles (green); (d) For every profile-point P, $z$-coordinates are averaged in the surrounding area $\Delta_x\Delta_y$; and (e) profile and parameters for calculation of roughness index.

proposed:

$$R_s = \frac{2}{f_c^{1/8}} \tag{3}$$

where $f_c$ is expressed in [MPa]. Fig. 11 compares Eq. (3) with the $R_s$ values for surfaces from the literature and the scans from the present experimental programme, classified according to the failure mode. Considering the variability of concrete, this comparison shows a relatively good match between Eq. 3 and the test results presented in this paper, which are, however, subjected to some level of scatter. This can be explained by the fact that the tested surfaces were relatively small and thus subjected to greater variability compared to the more average estimate of Eq. 3. The figure confirms in any case that simplified approaches for estimating the concrete roughness only based on the maximum aggregate size $D_{max}$ [23,9,6] should be improved by also accounting for the influence of the concrete strength.

4. The absolute value $\Delta_{z,max} = z_{max} - z_{min}$ (top and bottom points of the surface, see Fig. 9).

The calculated values for the investigated surfaces of the various indexes are reported in Table 4 and summarized in Fig. 12. From the various indexes and values (see Fig. 12), the following observations can be made:

- Consistent agreement is found between $R_p$, $R_s$ and $\Delta_{z,max}$. PC corresponds to the lowest values of these indexes, that increase consistently for NDSC and DSC.
- Larger aggregate sizes correspond to higher roughness indexes.
- A limited percentage of steep segments (related to higher values of $R_p$ and $R_s$) seems sufficient to develop high contact forces and usually leads to DSC failures (particularly for values of $R_p$ above 1.15)

**Table 4**
Measured values of various roughness indicators.

| # | Failure | $R_p$ [–] | $R_s$ [–] | $\Delta_{z,max}$ [mm] |
|---|---|---|---|---|
| 021501 | DSC* | 1.21 | 1.35 | 9.65 |
| 021601 | NDSC | 1.20 | 1.25 | 7.50 |
| 022002 | NDSC | 1.21 | 1.34 | 7.60 |
| 022101 | DSC | 1.25 | 1.43 | 10.61 |
| 022102 | NDSC | 1.18 | 1.30 | 9.19 |
| 030101 | DSC | 1.29 | 1.43 | 9.35 |
| 030201 | DSC | 1.18 | 1.25 | 8.06 |
| 030802 | PC | 1.16 | 1.25 | 8.74 |
| 030901 | PC | 1.14 | 1.21 | 7.00 |
| 040501 | NDSC | 1.13 | 1.27 | 5.88 |
| 040601 | NDSC | 1.16 | 1.26 | 7.79 |
| 050101 | DSC | 1.25 | 1.39 | 10.37 |
| 050102 | NDSC | 1.16 | 1.27 | 8.43 |
| 050202 | DSC* | 1.16 | 1.24 | 7.74 |
| 050301 | PC | 1.15 | 1.22 | 7.37 |
| 050302 | NDSC | 1.15 | 1.22 | 6.61 |
| 050401 | NDSC | 1.15 | 1.23 | 8.77 |
| 050801 | NDSC | 1.14 | 1.21 | 7.52 |
| 050802 | DSC | 1.32 | 1.40 | 8.30 |
| 050902 | NDSC | 1.18 | 1.31 | 6.80 |
| 070101 | PC | 1.11 | 1.18 | 8.67 |
| 070302 | DSC | 1.22 | 1.32 | 9.16 |
| 070501 | DSC | 1.16 | 1.26 | 8.98 |
| 070601 | NDSC | 1.12 | 1.19 | 6.62 |
| 070902 | PC | 1.15 | 1.21 | 5.27 |
| 071401 | PC | 1.10 | 1.15 | 6.54 |

## 3. Consistent modelling of transfer of forces through cracked concrete

The modelling approaches for aggregate interlock proposed by Walraven [39] (see Appendix A) and Li et al. [21] (see Appendix B)

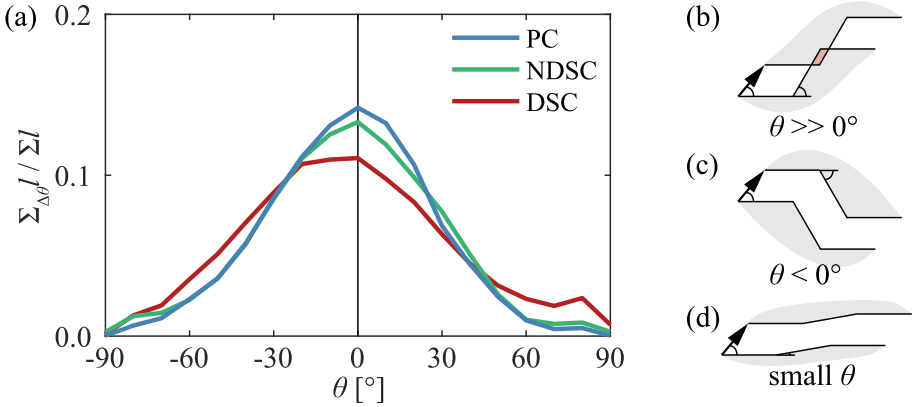


**Fig. 10.** Influence of angles $\theta$ (a) Average distributions, classified by failure mode; (b) segment with large $\theta$ (in contact); (c) segment with $\theta < 0°$ (no contact); and (d) segment with small $\theta$ (no contact).

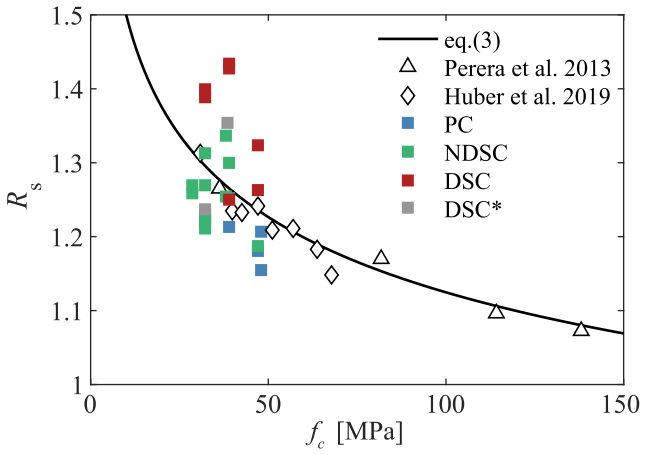


**Fig. 11.** Comparison of measured $R_s$ values with Eq. (3) and tests from the literature [17,29].

focus on the transfer of forces due to interface contacts and provide good estimates for tests resulting in PC and NDSC. However, they are not addressed at cases governed by DSC, which are observed in some full scale structures like concrete beams without transversal reinforcement failing in shear [4]. Moreover, since they were mostly calibrated on specimens pre-cracked by splitting, and with limited control over the initial crack opening, these models do not account for the potential of cracked concrete to transfer tensile and shear stresses due to residual material tensile resistance and soundness. This residual tensile strength of concrete cracks is observed in Mode I tests [36], and the phenomenon is also considered in models for shear transfer in beams [6] and punching of slabs [34]. Hillerborg [14] explained the residual tensile strength of concrete for small deformations by introducing the concept of the *fracture process zone*. Such zones are characterized by localized, but not fully developed, cracking, and possess the capacity to transfer forces due to the material bridging the discontinuity. This effect is actually not negligible in the local transfer of forces at a crack and shall also be accounted for to formulate a more comprehensive approach to the phenomenon.

The model presented hereafter is grounded on the approach of Li et al. [21] with respect to the consideration of contacts between crack lips, but accounts also for the residual material strength of cracks which are not fully developed. Such an approach is applicable to cases with monotonic loading resulting in PC, NDSC and DSC, as will be shown through a comparison with the experiments, and suitably reproduces the complete load–displacement response of the specimens, including their softening branch.

### 3.1. Model outline

The surface roughness is used as an input parameter using the parallel profiles obtained from the final failure surface as described in Section 2.4 (or any analytical function for it). The contact state is calculated at each point as a function of the profile-geometry and the externally applied kinematics. In particular, the local effective penetration $p$ is determined for each segment and load-step (see Section 3.1.1). Two cases can result:

1. The segment is penetrating material on the opposite crack-side. The procedure outlined in Section 3.1.2 is applied to determine the contact forces.
2. The segment is separated from the opposite crack-side, but can still transfer forces due to the residual soundness of the fracture process zone. The procedure outlined in Section 3.1.3 is thus applied.

#### 3.1.1. Contact events

In order to determine the occurrence of a contact, the model considers that the segments at each side of a crack behave as solid (undeformable) bodies. A 2D analysis will be performed, considering $x$ as the horizontal axis and $y$ as the vertical one (previously referred to as $z$-axis in the 3D roughness analysis of Section 2.4). By imposing the displacements resulting from the crack kinematics ($u_x$, $u_y$) (see Fig. 13a) at each point, the location of the displaced segment can be derived (Fig. 13c). On that basis, an auxiliary geometric parameter $p$ can be calculated, related to the local material penetration. When this parameter is positive ($p > 0$ in Fig. 13c), the two sides of the crack are not in contact. When it turns negative ($p < 0$, red areas in Fig. 13c), the two areas overlap and contact forces develop. This procedure is simple and efficient to apply (alternative approaches based on the local opening could be used [31]). It allows in addition the calculation of local opening and sliding of a segment $i$ ($\delta_i$ and $w_i$ calculated according to the segment direction, refer to Fig. 13b) as:

$$\begin{bmatrix} \delta_i \\ w_i \end{bmatrix} = \begin{bmatrix} \cos(\theta_i) & \sin(\theta_i) \\ -\sin(\theta_i) & \cos(\theta_i) \end{bmatrix} \begin{bmatrix} u_x \\ u_y \end{bmatrix} \tag{4}$$

It can be noted that in fact, the sides of the crack are not rigid but also deform during the loading process. Consideration of this issue will not be included for simplicity reasons, but can be consulted in [31].

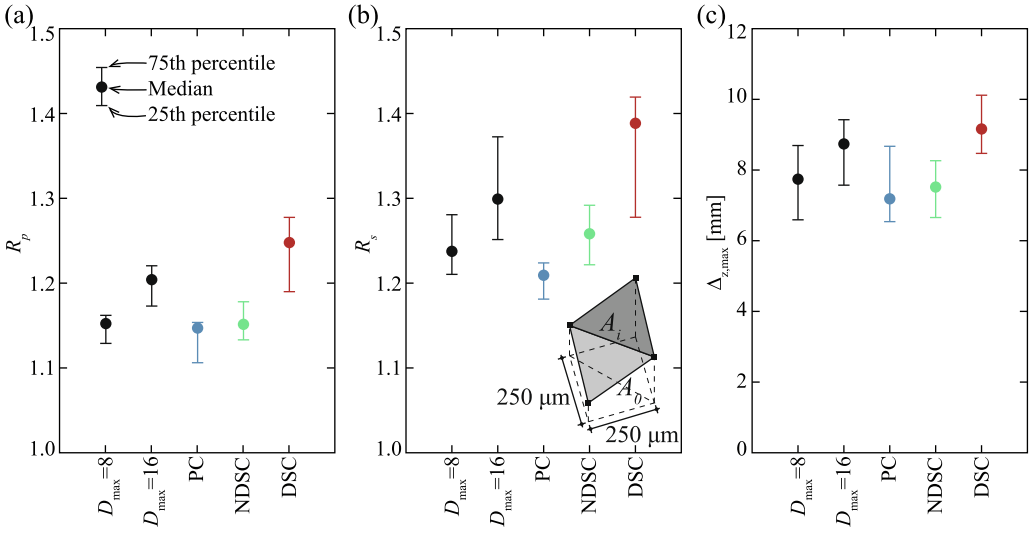


**Fig. 12.** Distribution of various roughness indicators: (a) $R_p$; (b) $R_s$; and (c) $\Delta_{z,max}$.

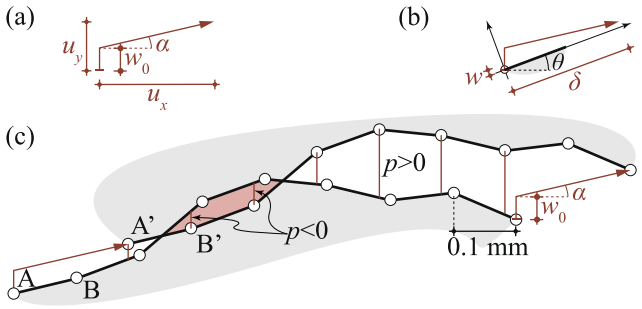


**Fig. 13.** Calculation of contact properties: (a) projection of kinematics on global coordinate system; (b) projection of kinematics on local coordinate system corresponding to a segment; and (c) procedure to calculate $p$.

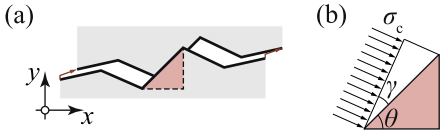


**Fig. 14.** Modelling of penetrating segments; (a) Crack profile in contact under the applied kinematics; and (b) contact stress acting on interface.

### 3.1.2. Penetrating segments

When $p_{ij} \leqslant 0$, the segment $i$ is penetrating the opposite side of the crack during load-step $j$ (see Fig. 14a) and the procedure described in this section is followed. The contact compressive stress $\sigma_{c,ij}$ acting on the crack interface is calculated using an elastic–plastic constitutive law expressed by:

$$\sigma_{c,ij} = 343 f_c^{1/3} |w_{ij}| \leqslant \eta_c f_c \qquad [\text{MPa}] \tag{5}$$

where $f_c$ is the compressive strength of concrete in [MPa] and $w$ is the crack opening in [mm]. The elastic part was originally introduced in [21], while limiting the contact stresses to a maximum of $\eta_c f_c$ is necessary to account for the material crushing strength. The parameter $\eta_c$ accounts for the effective concrete resistance and depends upon two phenomena: the brittleness of concrete in compression and the enhancement of the resistance (and toughness) under confined conditions. The general formulation of the factor $\eta_c$ thus results:

$$\eta_c = \eta_{f_c} + \eta_{\text{conf}} \tag{6}$$

The brittleness of concrete in compression can be considered by means of a brittleness coefficient $\eta_{f_c}$ accounting for potential stress redistributions. This expression considers that an enhanced material brittleness (characterized in a global manner by the material compressive strength) leads to higher decreases of overall strength when some regions soften while others attain their peak strength. According to [22], this coefficient can be evaluated as $\eta_{f_c} = \left(\frac{30[\text{MPa}]}{f_c}\right)^{1/3} \leqslant 1$ (see also [9]). The second parameter ($\eta_{\text{conf}}$) accounts for the enhanced strength and material toughness under confined conditions [26]. Such enhancement of the strength is proposed to be approximated by the following expression:

$$\eta_{\text{conf}} = 3 - 11(R_p - 1) \geqslant 0 \tag{7}$$

where $R_p \geqslant 1$ is calculated using Eq. 1. The confinement effect in contact regions is considered to be higher for low values of $R_p$ because in this case fewer contacts occur [30], leading to relatively isolated zones of concrete crushing (high confinement stresses can develop due to the undamaged material surrounding the contact area). For rougher surfaces, on the contrary, the contacts increase in number, resulting in more damaged areas and lower levels of confinement around them. On this basis, the expression for $\eta_{\text{conf}}$ was fitted in accordance to the experimental results. Further work in this field should however lead to a more refined approach for this expression.

With respect to the inclination of the contact forces, they might not develop perpendicular to the surface, refer to angle $\gamma$ in Fig. 14b. This angle is taken as 0° in [21], implying that no friction acts on the surface. However, as pointed out in previous studies [40], some friction is likely to be present. It can be noted that the local value $\gamma$ has influence on the overall relationship between $\tau$ and $\sigma$, as discussed in Section 2.3. For example, Mode II tests tend to result in similar values of $\tau$ and $\sigma$, while in Mixed-Mode tests with large values of $\alpha$, $\tau$ is generally larger than $\sigma$. In the absence of more specific data, and in accordance to the test results later presented, a constant value of $\gamma = 10°$ will be adopted in the following. However, it should be considered that $\gamma$ can need some future research and adjustment for different kinematics (potentially varying as a function of parameter $\psi$ discussed with Fig. 8). On this basis, for a unitary length, it results (Fig. 14b):

$$(\sigma, \tau)_{\text{P},ij} = (-\sigma_{c,ij}\cos^2(\gamma),\ \ \sigma_{c,ij}\sin(\gamma)\cos(\gamma)) \tag{8}$$

Once the stresses acting on the crack interface are determined, they are eventually rotated to the global coordinate system, deriving the contribution of each segment in contact to the total transferred force.

### 3.1.3. Contribution of residual strength

In cases of positive crack opening ($p_{ij} > 0$, crack separation) and for small openings, there is a potential for some residual resistance due to material bridging and thus a capability to transfer forces. The total transferred force can be directly related to the residual tensile strength of concrete and thus to the level of crack opening. This contribution is estimated using the following equation in accordance to the experimental evidence presented in this paper:

$$(\sigma, \tau)_{\text{S},ij} = (-\nu_{\sigma,ij} f_{ct},\ \ \nu_{\tau,ij}\sqrt{f_c}) S_{ij} \tag{9}$$

where $f_c$, $f_{ct}$, $\sigma$ and $\tau$ are expressed in [MPa]. The dimensionless parameter $S$ accounts for the material soundness, with $S = 1$ referring to undamaged material conditions and $S = 0$ for a fully damaged material. This soundness parameter can be estimated using a similar expression as for the Mode I residual tensile strength of concrete but with generalized parameters. Various expressions can be found in the literature for this purpose, as for example those proposed by Reinhardt [33] or Ng et al. [25]. In this investigation, the equation proposed by Hordijk [15] for Mode I residual tensile strength will be generalized as follows:

$$S_{ij} = (1 + (c_1 u_{M,ij}/w_c)^3) e^{-c_2(u_{M,ij}/w_c)} - u_{M,ij}/w_c (1 + c_1^3) e^{-c_2},\ \ S_{ij} \geqslant 0 \tag{10}$$

According to its original formulation [15], the values $c_1 = 3$, $c_2 = 6.93$ and $w_c = 5.14\frac{G_F}{f_{ct}} = 5.14\frac{0.073 f_c^{0.18}}{0.3 f_c^{2/3}}$ [mm] can be adopted ($w_c$, $G_F$ and $f_{ct}$ are determined in accordance to [6,9,15]). With respect to parameter $u_M$, it accounts for the considered kinematics. Since the original formulation was developed for Mode I, the kinematics is characterized only by the opening of the crack ($u_M = w$). In the present case, it is assumed that a similar approach is also valid for a Mixed-Mode case, by using a generalized displacement parameter whose value is calculated as:

$$u_{M,ij} = \sqrt{w_{ij}^2 + (0.3\delta_{ij})^2} \quad [\text{mm}] \tag{11}$$

where $w$ is the opening normal to the crack and $\delta$ its relative sliding. This assumption allows accounting for the additional damage due to crack sliding in the fracture process zone although to a lesser degree compared to the crack opening (the value of coefficient 0.3 was selected as a reasonable average estimate finely fitting test results, but could be tailored in specific cases related to the local shear strength of material). As can be noted, the material strength (correlated to $f_{ct}$ in pure tension and to $\sqrt{f_c}$ in pure shear [9]) is reduced for larger openings and for sliding of the FPZ.

The dimensionless parameters $\nu$ of Eq. (9) are functions of $\delta$, as they consider the increasing potential for force transfer due to material bridging as crack-sliding increases (enhanced number of contacts). For

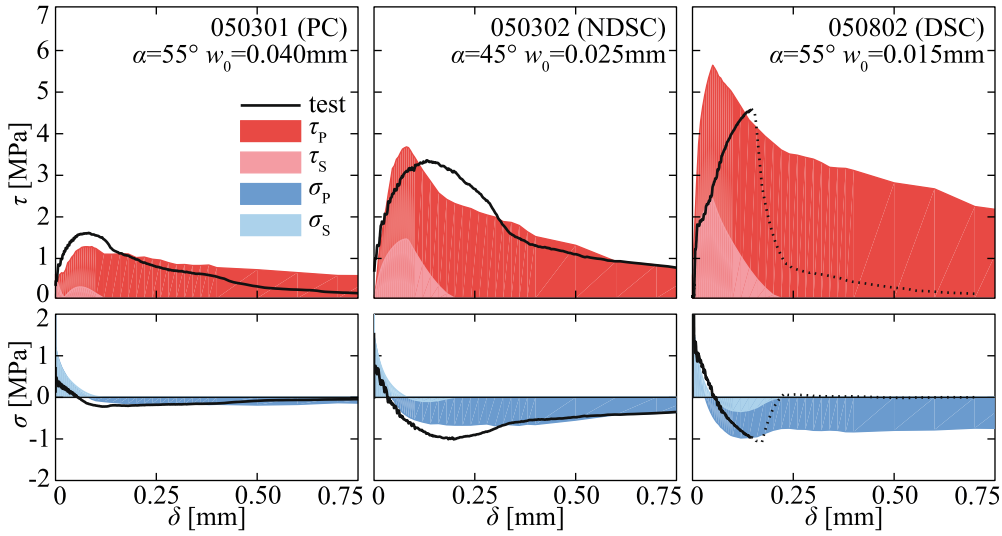


**Fig. 15.** Comparison of model estimates with experimental results for three tests with varying failure mode (subscript P indicates contributions due to penetrating segments, while subscript S indicates the contribution of the residual tensile strength).

the parameter $\nu_\sigma$, accounting for the activation of normal forces, the following equation is proposed:

$$\nu_{\sigma,ij} = 1 - \left(100\frac{\delta_{ij}}{D_{\max}}\right) \geqslant -2 \qquad [-] \tag{12}$$

This equation is justified by the fact that when $\delta$ increases, the normal stresses turn from tension values ($\nu_\sigma > 0$) to compressive ones ($\nu_\sigma < 0$, refer to experimental results later discussed in Fig. 15).

With respect to parameter $\nu_\tau$, it accounts for the activation of the friction forces in rough surfaces of the fracture process zone. It varies between 0 and 2, to consider that the local stresses increase for larger sliding (enhanced activation of bridging material), and is proposed to be evaluated as:

$$\nu_{\tau,ij} = 200\frac{|\delta_{ij}|}{D_{\max}} \leqslant 2 \qquad [-] \tag{13}$$

The expressions proposed (Eqs. (10)–(13)) show overall good agreement when compared to test results. They have been selected to provide a consistent transition to pure Mode I and to fit reasonably the experimental results presented in this article. Nevertheless, further work is needed to consolidate them and to better clarify their limits of applicability.

### 3.2. Model results

By summing both contributions (regions under penetration or separation), the total transferred force can be calculated. Fig. 15 reports the model estimates for three representative tests with different failure modes and compares them to the experimental results (marked with a dotted line when the development of a DSC did not allow to respect the imposed kinematics). Further details are given in Table 5, where the maximum shear stresses of several models are also compared with the experimental values (2PM, referring to the Two-Phase Model by Walraven [39] according to the fitted expressions given in [6] and *fib* referring to *fib*'s Model Code 2010, Eqs. 5.1–48 and 5.1–49 [9]). As it can be noted, the proposed approach yields a reasonable agreement for almost all specimens. Such consistency is found both in terms of maximum strength and deformation at peak load, and is better than for the other investigated models (Table 5). The post-peak response is also reasonably reproduced, particularly for PC and NDSC, but the residual strength is normally overestimated for DSC. A significant amount of scatter can still be observed, which can be explained by the very limited crack surface of the tests (measuring approximately 1000 mm$^2$). In actual cases, the contributions are averaged over a significantly larger surface, thus leading to a reduction of the scatter.

With respect to the contributions due to penetration (P) and the residual tensile strength of the fracture process zone (separation S) to the overall strength, Fig. 16 presents the results of two specimens failing by DSC. It can be noted that in one case (Fig. 16a, associated with a large initial crack opening), the forces almost exclusively derive from penetrating segments, while in the other (Fig. 16b, associated with a lower initial crack opening), the governing contribution is that of the residual tensile strength. This shows that both contributions are necessary to consistently reproduce the phenomenon in a general manner and that the fracture process zone can govern for low crack widths. The plots for all experiments are reported in Appendix C. It can be noted from these results that long post-peak softening phases are mainly governed by penetrating material parts engaging contacts. Also, it can be noted that the contribution of the fracture process zone has a significant influence on the failure mode and transferred forces, particularly at low displacement levels.

More details on the role of the different contributions are presented in Fig. 17 for all tests. Although subjected to a significant scatter, it can be observed that rougher surfaces (associated with higher values of $R_p$ and to DSC failure mode) yield to higher resistances and tend to be dominated by contacts due to material penetration. On the contrary, smoother surfaces (associated with lower values of $R_p$ and PC failure modes) yield to lower resistances and tend to be highly dependant on the contribution of the residual tensile strength.

The relevance of the development of dominant secondary cracking shown in the experiments can be related to the fact that the protruding material has relatively large protuberances compared to the tested region. In particular cases, as for beams without transverse reinforcement failing in shear, this can be associated with the engagement of meso-roughness (large zones with steeper inclination, Fig. 1c, see [4]). Otherwise, a small region of protruding material engages secondary cracks which develop in a potentially stable manner, as a redistribution of stresses to other regions is possible. In these cases, the global behaviour can be observed to be less governed by secondary cracking considering the average response of the phenomenon.

Finally, Fig. 18a shows that the peak values $\tau_{\max}$ calculated with the proposed model suitably account for the influence of surface roughness (characterized by the parameter $R_p$) with no marked trend in the results. As it can be noted, the material roughness is the most reliable indicator for the type of failure observed (with low roughness associated with PC and higher roughness associated with DSC). Neglecting

**Table 5**
Summary of results: ratios of values obtained experimentally and by modelling; "exp" refers to test values, "mod" to the proposed model, "2PM" to the equations in Appendix A for a Two-Phase Model [6] (fitted on the basis of the formulation by Walraven [40]) and "*fib*" to the Eqs. (5.1–48, 5.1–49) in *fib*'s Model Code 2010 [9]

| | | exp/mod | | | exp/2PM | | | exp/*fib* | | |
|---|---|---|---|---|---|---|---|---|---|---|
| # | Failure | $\tau_{max}$ | $\sigma_{min}$ | $\delta(\tau_{max})$ | $\tau_{max}$ | $\sigma_{min}$ | $\delta(\tau_{max})$ | $\tau_{max}$ | $\sigma_{min}$ | $\delta(\tau_{max})$ |
| 30802 | PC | 0.69 | 0.00 | 0.35 | 1.01 | 0.00 | 0.39 | 0.54 | 0.00 | 0.29 |
| 30901 | PC | 0.97 | 0.00 | 0.33 | 0.59 | 0.00 | 0.28 | 0.35 | 0.00 | 0.21 |
| 50301 | PC | 1.26 | 1.15 | 0.91 | 1.14 | 0.82 | 0.83 | 0.61 | 0.41 | 0.35 |
| 70101 | PC | 0.71 | -0.21 | - | 0.82 | -0.15 | 0.29 | 0.45 | 0.12 | 0.13 |
| 70902 | PC | 0.74 | 1.15 | 3.82 | 1.42 | 2.04 | 3.92 | 0.95 | 1.77 | 0.76 |
| 71401 | PC | 1.72 | 2.21 | 0.55 | 0.80 | 0.58 | 0.72 | 0.53 | 0.35 | 0.15 |
| AVG | PC | 1.02 | 0.72 | 1.19 | 0.96 | 0.55 | 1.07 | 0.57 | 0.44 | 0.32 |
| COV | PC | 0.40 | 1.32 | 1.25 | 0.31 | 1.50 | 1.32 | 0.36 | 1.52 | 0.75 |
| 21601 | NDSC | 0.50 | 0.35 | 0.47 | 0.81 | 0.50 | 0.85 | 0.55 | 0.29 | 0.30 |
| 22002 | NDSC | 1.13 | 1.33 | 0.95 | 1.18 | 1.08 | 1.50 | 0.93 | 0.69 | 0.32 |
| 22102 | NDSC | 0.97 | 0.50 | 0.73 | 0.85 | 0.44 | 0.42 | 0.52 | 0.21 | 0.21 |
| 40501 | NDSC | 0.46 | 0.42 | 1.90 | 0.91 | 0.80 | 1.71 | 0.66 | 0.38 | 0.33 |
| 40601 | NDSC | 0.90 | 0.71 | 3.03 | 1.78 | 1.50 | 2.01 | 1.18 | 0.68 | 0.51 |
| 50102 | NDSC | 0.90 | 0.91 | 2.83 | 1.84 | 1.81 | 1.52 | 1.13 | 0.83 | 0.48 |
| 50302 | NDSC | 0.91 | 1.48 | 1.65 | 1.14 | 1.15 | 1.23 | 0.73 | 0.54 | 0.41 |
| 50401 | NDSC | 1.06 | 0.57 | 0.61 | 1.01 | 0.44 | 0.40 | 0.55 | 0.17 | 0.17 |
| 50801 | NDSC | 1.28 | 2.29 | 3.28 | 2.14 | 2.41 | 0.80 | 0.93 | 0.71 | 0.50 |
| 50902 | NDSC | 0.43 | 0.28 | 1.41 | 0.79 | 0.59 | 1.41 | 0.56 | 0.30 | 0.28 |
| 70601 | NDSC | 1.65 | 0.25 | 3.15 | 0.98 | 0.28 | 0.46 | 0.41 | 0.12 | 0.31 |
| AVG | NDSC | 0.93 | 0.83 | 1.82 | 1.22 | 1.00 | 1.12 | 0.74 | 0.45 | 0.35 |
| COV | NDSC | 0.40 | 0.77 | 0.60 | 0.39 | 0.67 | 0.50 | 0.35 | 0.56 | 0.33 |
| 21501 | DSC* | 1.12 | 0.80 | 0.93 | 1.63 | 1.15 | 0.62 | 1.06 | 0.59 | 0.33 |
| 22101 | DSC | 1.10 | 1.04 | 1.00 | 2.54 | 2.62 | 0.77 | 1.34 | 0.92 | 0.58 |
| 30101 | DSC | 0.66 | 0.42 | 1.33 | 3.80 | 3.69 | 1.62 | 2.24 | -1.11 | 1.22 |
| 30201 | DSC | 1.36 | 1.38 | 1.63 | 1.90 | 1.41 | 0.94 | 1.16 | 0.67 | 0.47 |
| 50101 | DSC | 1.41 | 0.87 | 1.32 | 3.31 | 3.30 | 0.76 | 1.44 | 0.85 | 0.48 |
| 50202 | DSC* | 1.25 | 1.26 | 1.56 | 1.65 | 1.73 | 2.28 | 1.21 | 0.90 | 0.49 |
| 50802 | DSC | 0.81 | 1.0 | 2.92 | 2.22 | 2.42 | 3.74 | 1.58 | 1.41 | 0.69 |
| 70302 | DSC | 1.00 | 0.94 | 2.61 | 2.43 | 2.69 | 2.68 | 1.63 | 2.28 | 0.52 |
| 70501 | DSC | 0.77 | 0.53 | 3.89 | 2.82 | 2.90 | 1.23 | 1.55 | -2.30 | 0.53 |
| AVG | DSC | 1.05 | 0.91 | 1.91 | 2.48 | 2.43 | 1.63 | 1.47 | 0.47 | 0.59 |
| COV | DSC | 0.25 | 0.34 | 0.53 | 0.30 | 0.35 | 0.66 | 0.24 | 2.92 | 0.43 |
| AVG | all | 0.99 | 0.83 | 1.73 | 1.60 | 1.39 | 1.28 | 0.95 | 0.45 | 0.42 |
| COV | all | 0.34 | 0.74 | 0.65 | 0.53 | 0.78 | 0.76 | 0.50 | 1.87 | 0.54 |

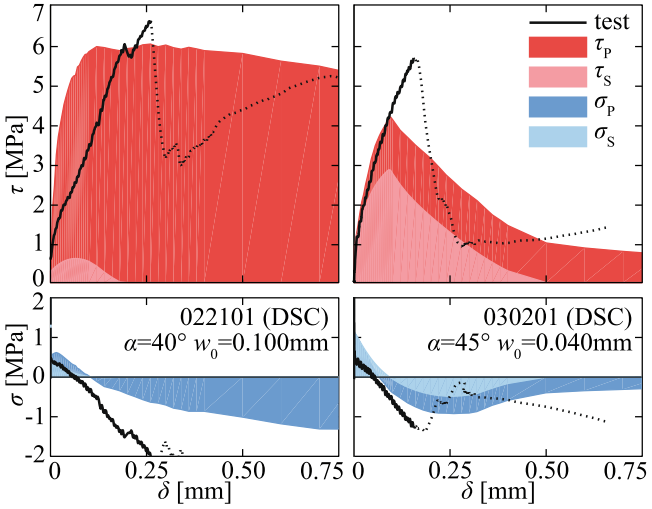


**Fig. 16.** Two tests with DSC and different relative contributions from contacts in penetration (subscript P) and separation (subscript S).

the role of this parameter, as for instance performed in the equations for aggregate interlocking proposed by Cavagnis et al. [6] (fitted on the basis of the Two-Phase Model of Walraven [40]) yields however to a clear trend (see Fig. 18b), with a consistent underestimation of the transferred load for increasing values of the surface roughness. Such approaches are thus in principle suitable for the range of $R_p$ corresponding to PC or NDSC failure modes (see Fig. 18b). A correction of the equations by Cavagnis et al. [6] to account for this effect is presented in Appendix D. It shall also be highlighted that all expressions provided in this manuscript have been verified for the range of experiments available and presented, but future work is required to consolidate its application to other cases (high-strength concrete, cyclic response…).

## 4. Conclusions

This paper investigates the transfer of forces through cracked concrete by means of a review of the phenomenon at micro-structural level. The results of a specific testing programme are presented as well as a comprehensive modelling frame for the phenomenon. The main conclusions of this investigation are summarized below:

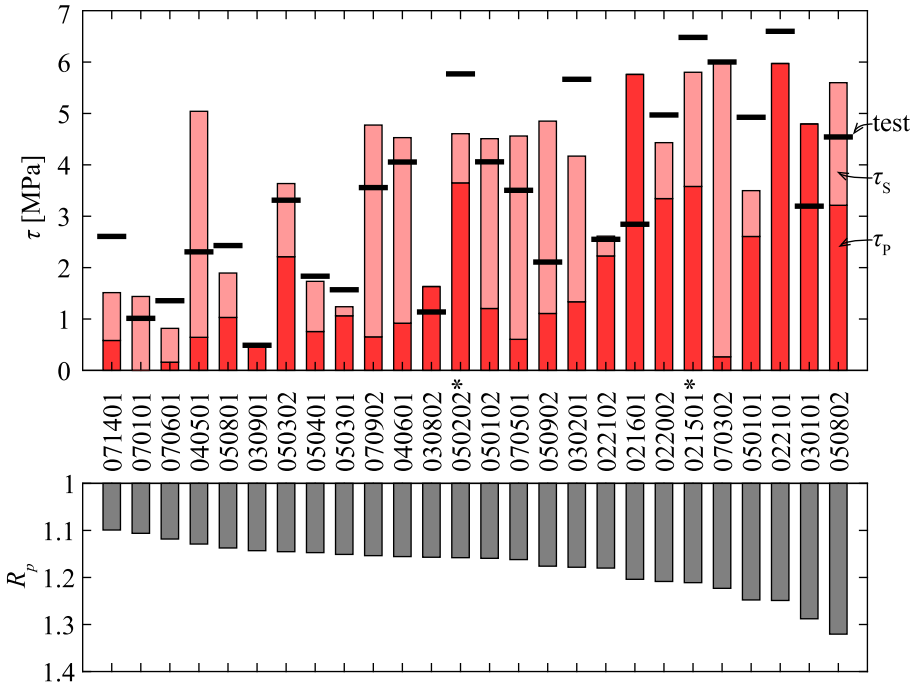


**Fig. 17.** Model contributions, ordered by surface roughness $R_p$.

1. The actual roughness of the crack surface plays a major role in the failure mode and capacity to transfer shear forces. Notably, the presence of steep segments engaging large contact forces can govern the response and observed failure mode.
2. For the considered surfaces, the crack surface roughness is related to the concrete strength and the maximum aggregate size.
3. In some tests, the development of secondary cracks at an angle of approximately 45° to the primary crack has been observed.
4. The development of secondary cracks is usually associated with rough surfaces characterized by an increased amount of steep segments or by flat kinematics resulting in significant amounts of material engagement.
5. Other than forces developed due to direct contacts, a significant amount of force can potentially be transferred by the residual tensile strength of concrete both in tension and shear.
6. Consistent modelling of the phenomenon of transfer of forces through cracked concrete can be performed on the basis of these ideas. A model for this purpose is presented in this paper, showing better performance than classical approaches and allowing to determine the amount of force transferred by penetration and separation and applicable for all potential failure modes.

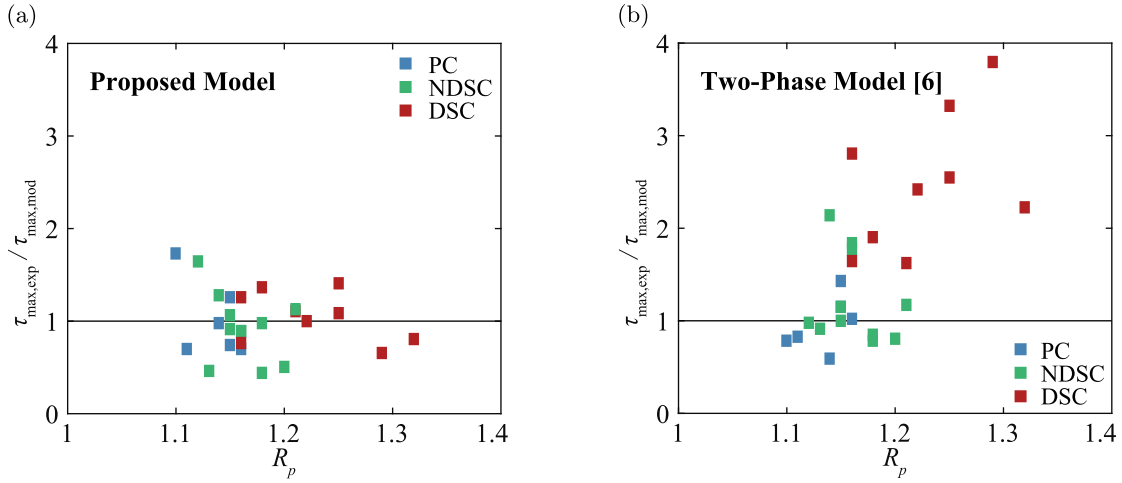


**Fig. 18.** Peak values $\tau_{max}$ as a function of the roughness index $R_p$: (a) Proposed model; and (b) Two-Phase-Model.

## CRediT authorship contribution statement

**Max Tirassa:** Conceptualization, Methodology, Software, Investigation, Formal analysis, Writing - original draft, Visualization, Project administration, Validation, Resources, Data curation. **Miguel Fernández Ruiz:** Conceptualization, Methodology, Investigation, Formal analysis, Writing - original draft, Writing - review & editing, Visualization, Supervision, Project administration, Funding acquisition, Validation. **Aurelio Muttoni:** Conceptualization, Methodology, Investigation, Formal analysis, Writing - review & editing, Visualization, Supervision, Project administration, Funding acquisition, Validation.

## Declaration of Competing Interest

The authors declare that they have no known competing financial interests or personal relationships that could have appeared to influence the work reported in this paper.

## Acknowledgements

This work has been funded by the Swiss National Science Foundation, research grant 200021_169649. The authors are very appreciative of the support received.

The authors also thank Professor Frank J. Vecchio from the University of Toronto, for his review and comments in drafting the manuscript.

## Appendix A. Two-Phase Model and simplified expressions based on it

The Two-Phase Model [39,40] idealizes concrete at the meso-scale as a material consisting of rigid, spherical aggregates surrounded by a perfectly plastic cement matrix. Cracks are considered as planar with protruding aggregates. If the system is subjected to sliding, the aggregates can engage the opposite side and transfer forces through aggregate-matrix contact. Under these assumptions, the Two-Phase Model considers the surface as consisting of 2D-profiles parallel to the loading direction, similar to the ones of Section 2.4. Using stochastic considerations for the granulometric distribution of aggregates it is possible to calculate the overall contact area. Finally, the model considers a rigid-plastic constitutive material law and a constant friction coefficient to account for the inclination of the force resulting at each contact. The Two-Phase Model has constituted one of the most comprehensive and consistent approaches for dealing with aggregate interlock issues. Despite its limitations [31] its principles have been successfully adopted to shear [4,38] and punching shear [11] cases.

The original formulation of the Two-Phase Model has further been adapted to various kinematics and recently analytical expressions have been proposed by Cavagnis et al. [6] fitting the predictions of the Two-Phase Model but simple enough to be integrated analytically:

$$\tau = \sqrt{f_c}\frac{c_3\overline{\delta}^{4/3}}{(c_2\overline{w})^{1.8+c_2\overline{\delta}}} \tag{A.1a}$$

$$\sigma = \sigma_{res} - \sqrt{f_c}\frac{c_4\overline{\delta}^{4/3}}{(c_2\overline{w})^{3+c_2\overline{\delta}}} \tag{A.1b}$$

where $\sigma_{res} = f_{ct}(1-(w/w_c)^{c_1}) \geqslant 0$ is the residual tensile strength of concrete measured in [MPa], $c_1 = 0.31$, $c_2 = 40$, $c_3 = 35$ and $c_4 = 400$ are constants, $w_c = \frac{G_F}{f_{ct}}\frac{1+c_1}{c_1}$ is the value of crack opening in [mm] for which the residual tensile resistance vanishes [33], $G_F = 0.073f_c^{0.18}$ is the fracture energy in [MPa], $f_{ct}$ is the tensile resistance of concrete calculated as $f_{ct} = 0.3f_c^{2/3}$ [MPa], $f_c < 50$ MPa and $f_{ct} = 0.3(50f_c)^{1/3}$ [MPa] for $f_c \geqslant 50$ MPa, $\overline{\delta} = \delta/d_{ag}$ and $\overline{w} = w/d_{ag}$ are the normalized crack openings using an average roughness value depending on the maximum aggregate size as $d_{ag} = \min(40, 16 + D_{\max})$ for $f_c \leqslant 60$ MPa and $d_{ag} = \min(40, 16 + D_{\max}(60/f_c)^2)$ for $f_c > 60$ MPa.

## Appendix B. Contact Density Model

The Contact Density Model [1,21] idealizes the roughness of a concrete surface as a collection of segments (called *contact units*) each with a given inclination with respect to a horizontal crack plane. The geometry of these contact units can be obtained by scanning of the concrete surface as shown in Fig. 9. A contact density function is then adopted to represent the overall distribution of inclinations.

For every direction $\theta$, the model considers all the corresponding segments and calculates the local kinematics, determining the crack opening. If a contact is detected, an elastic–plastic material law is applied, and the resulting contact stress is considered to be normal to the segment. For monotonic loading paths, the following equations are obtained [21]:

$$\tau = g\left(\frac{\delta\sin^3\beta + w\cos^3\beta}{3} - \frac{\delta w}{3\sqrt{\delta^2+w^2}} + 0.5w_{lim}\cos^2\beta\right) \tag{B.1a}$$

$$\sigma = g\left(\frac{-\delta\cos^3\beta + w\sin^3\beta}{3} - w\sin\beta + \frac{\delta^2+2w^2}{3\sqrt{\delta^2+w^2}} + w_{lim}\left(\frac{\pi}{4} - \frac{\beta}{2} - \frac{\sin(2\beta)}{4}\right)\right) \tag{B.1b}$$

where $g = 0.5A_tR_sK(w)$, $A_t = 4/\pi$ [mm$^2$], $R_s = \frac{436}{A_t}f_c^{1/3}$ [MPa/mm$^3$], $w_{lim} = 0.04$ [mm], $\beta = \arcsin\left(\frac{w_{lim}\delta + w\sqrt{w^2+\delta^2-w_{lim}^2}}{w^2+\delta^2}\right)$ if $\delta \geqslant w_{lim}$ and $\beta = \frac{\pi}{2}$ if $\delta \leqslant w_{lim}$.

## Appendix C. Model results

See Fig. C.19.

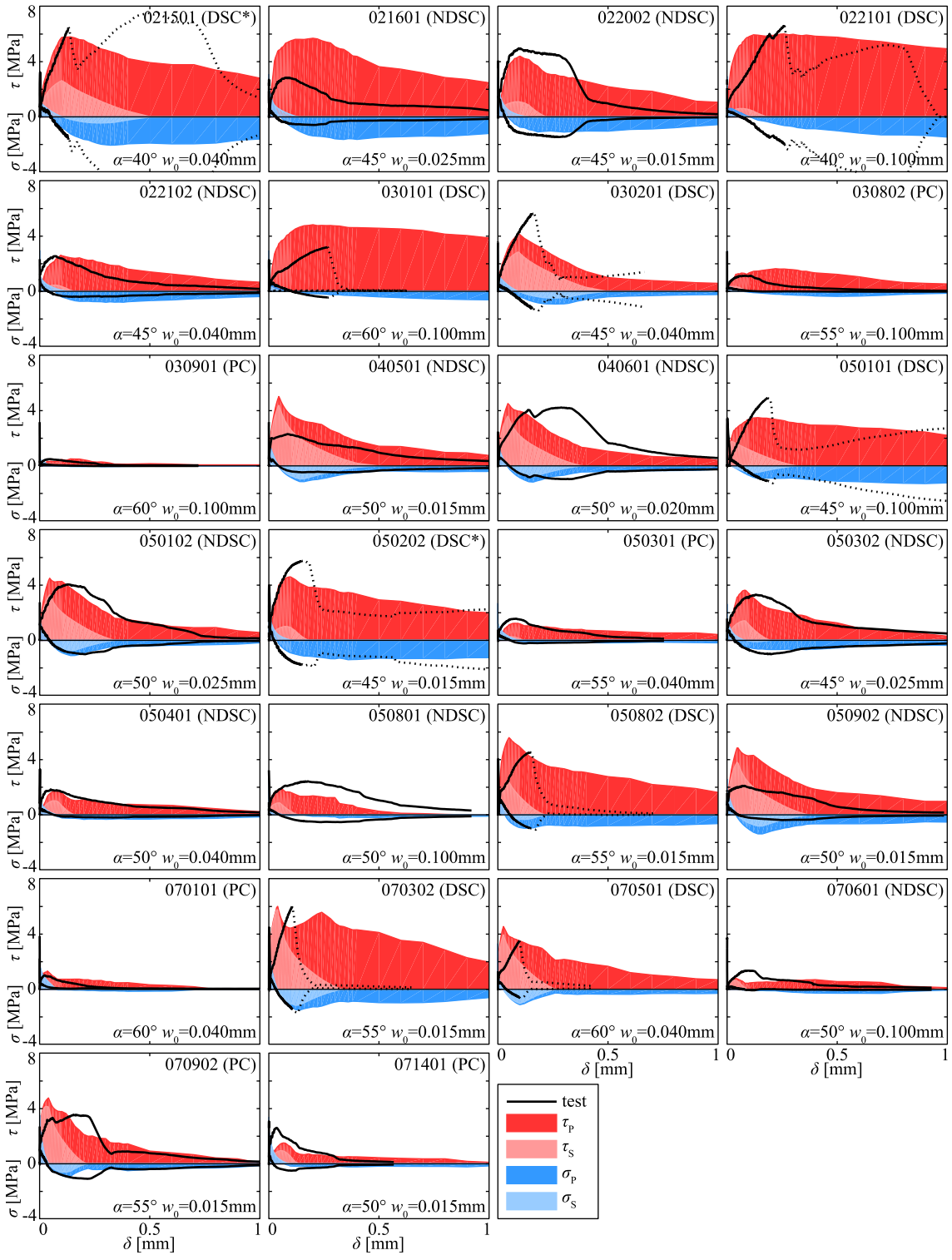


**Fig. C.19.** Comparison of model estimates with experimental results for all tests; dotted lines indicate that the global kinematics are not respected due to DSC.

## Appendix D. Parameter accounting for surface roughness

As shown in Fig. 18b, the results obtained with the approximated equations based on the Two-Phase Model from [6] and reported in Appendix A show a clear trend when plotted against the profile roughness index $R_p$. These equations can be modified to account for the surface roughness by introducing the following parameter:

$$\lambda_R = \left(\frac{R_p}{R_{p,\mathrm{ref}}}\right)^4 \leqslant 3, \quad R_{p,\mathrm{ref}} = 1.10 \tag{D.1}$$

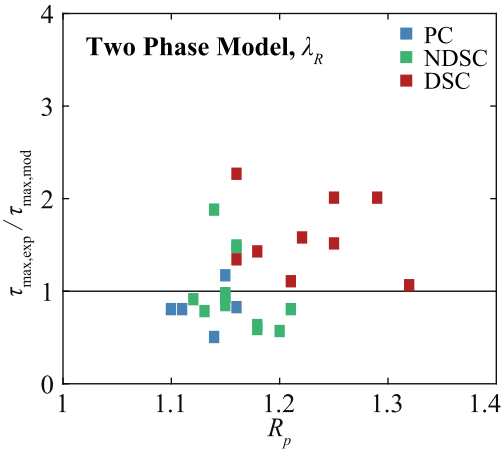


**Fig. D.20.** Peak values $\tau_{max}$ of Two-Phase-Model with parameter $\lambda_R$ as a function of the roughness index $R_p$.

**Table D.6**
Summary of model results; "2PM, $\lambda_R$" refers to results obtained with Eq. (D.2).

| | exp/(2PM, $\lambda_R$) | | |
|---|---|---|---|
| | $\tau_{max}$ | $\sigma_{min}$ | $\delta(\tau_{max})$ |
| AVG | 1.17 | 0.99 | 1.28 |
| COV | 0.42 | 0.72 | 0.76 |

The equations thus become:

$$\tau = \lambda_R \sqrt{f_c} \frac{c_3 \bar{\delta}^{4/3}}{(c_2 \bar{w})^{1.8+c_2\bar{\delta}}} \tag{D.2a}$$

$$\sigma = \sigma_{res} - \lambda_R \sqrt{f_c} \frac{c_4 \bar{\delta}^{4/3}}{(c_2 \bar{w})^{3+c_2\bar{\delta}}} \tag{D.2b}$$

with $\lambda_R$ increasing the estimates for surfaces which are significantly rougher than those of typical tests resulting in primary cracking, as can be seen in Fig. D.20 and Table D.6.

## Appendix E. Supplementary material

Supplementary data associated with this article can be found, in the online version, at https://doi.org/10.1016/j.engstruct.2020.111138.

## References


[1] Bujadham B, Mishima T, Maekawa K. Verification of the universal stress transfer model. Proc JSCE 1992;451/V-17:289–300.
[2] Calvi PM, Bentz EC, Collins MP. Pure mechanics crack model for shear stress transfer in cracked reinforced concrete. Struct J 2017;114:545–54.
[3] Carol I, Prat PC, López CM. Normal/shear cracking model: application to discrete crack analysis. J Eng Mech 1997;123:765–73.
[4] Cavagnis F, Fernández Ruiz M, Muttoni A. Shear failures in reinforced concrete members without transverse reinforcement: An analysis of the critical shear crack development on the basis of test results. Eng Struct 2015;103:157–73.
[5] Cavagnis F, Fernández Ruiz M, Muttoni A. An analysis of the shear-transfer actions in reinforced concrete members without transverse reinforcement based on refined experimental measurements. Struct Concrete 2017;19:49–64.
[6] Cavagnis F, Fernández Ruiz M, Muttoni A. A mechanical model for failures in shear of members without transverse reinforcement based on development of a critical shear crack. Eng Struct 2018;157:300–15.
[7] Cavagnis F, Simões JT, Ruiz MF, Muttoni A. Shear strength of members without transverse reinforcement based on development of critical shear crack. Struct J 2020;117:103–18.
[8] Divakar MP, Fafitis A, Shah SP. Constitutive model for shear transfer in cracked concrete. J Struct Eng 1987;113:1046–62.
[9] fib (International Federation for Structural Concrete). fib Model Code for Concrete structures 2010. Germany: Ernst & Sohn; 2013, 402 p.
[10] Giaccio G, Giovambattista A. Bleeding – evaluation of its effects on concrete behaviour. Mater Struct 1986;19:265–71.
[11] Guidotti R. Poinçonnement des planchers-dalles avec colonnes superposées fortement sollicitées. Ph.D. Thesis EPFL Lausanne Switzerland; 2010.
[12] Haeri H, Sarfarazi V, Lazemi HA. Experimental study of shear behavior of planar nonpersistent joint. Comput Concrete 2016;17:639–53.
[13] Hassanzadeh M. Behavior of fracture process zones in concrete influenced by simultaneously applied normal and shear displacements Ph.D Thesis Lund University Sweden; 1992.
[14] Hillerborg A. Analysis of one single crack. Fracture mechanics of concrete (developments in civil engineering). Amsterdam, Netherlands: Wittmann, Folker H; 1983. p. 223–49.
[15] Hordijk DA. Tensile and tensile fatigue behaviour of concrete; experiments, modelling and analyses. Heron 1992;37.
[16] Hsu TTC, Slate FO. Tensile bond strength between aggregate and cement paste or mortar. ACI J Proc 1963;60:465–86.
[17] Huber T, Huber P, Kollegger J. Influence of aggregate interlock on the shear resistance of reinforced concrete beams without stirrups. Eng Struct 2019;186:26–42.
[18] Issa MA, Issa MA, Islam MS, Chudnovsky A. Fractal dimension–a measure of fracture roughness and toughness of concrete. Eng Fract Mech 2003;70:125–37.
[19] Jacobsen JS. Constitutive mixed mode behavior of cracks in concrete: experimental investigations of material modeling. Ph.D. Thesis Technical University of Denmark Kongens Lyngby Denmark; 2012.
[20] Lange DA, Jennings HM, Shah SP. Relationship between fracture surface roughness and fracture behavior of cement paste and mortar. J Am Ceram Soc 1993;76:589–97.
[21] Li B, Maekawa K, Okamura H. Contact density model for stress transfer across cracks in concrete. J Faculty Eng Univ Tokyo 1989;40:9–52.
[22] Muttoni A. Die Anwendbarkeit der Plastizitätstheorie in der Bemessung von Stahlbeton. Ph.D. thesis ETH Zurich Switzerland; 1989.
[23] Muttoni A, Fernández Ruiz M. Shear strength of members without transverse reinforcement as function of critical shear crack width. ACI Struct J 2008;105:163–72.

[24] Muttoni A, Fernández Ruiz M, Simões JT. The theoretical principles of the critical shear crack theory for punching shear failures and derivation of consistent closed-form design expressions. Struct Concrete 2018;19:174–90.
[25] Ng TS, Htut TNS, Foster SJ. Fracture of steel fibre reinforced concrete-The unified variable engagement model. Technical Report R-460 School of Civil and Environmental Engineering. The University of New South Wales Sydney; 2012.
[26] Nielsen MP, Hoang LC. Limit analysis and concrete plasticity. 3rd ed. Boca Raton, Florida: CRC Press; 2011.
[27] Nooru-Mohamed MB. Mixed-mode fracture of concrete: an experimental approach Ph.D Thesis Delft University of Technology Delft Sweden; 1992.
[28] Paulay T, Loeber PJ. Shear Transfer By Aggregate Interlock. ACI Special Publ 1974;42:1–16.
[29] Perera SVTJ, Mutsuyoshi H. Shear behavior of reinforced high-strength concrete beams. ACI Struct J; Farmington Hills 2013;110:43–52.
[30] Pundir M, Anciaux G. Numerical generation and contact analysis of rough surfaces in concrete; 2020. Submitted for review, available on HAL: https://hal.archives-ouvertes.fr/hal-02573481.
[31] Pundir M, Tirassa M, Fernández Ruiz M, Muttoni A, Anciaux G. Review of fundamental assumptions of the Two-Phase model for aggregate interlocking in cracked concrete using numerical methods and experimental evidence. Cem Concrete Res 2019;125. 105855.
[32] Randl N. Design recommendations for interface shear transfer in fib Model Code 2010. Struct Concrete 2013;14:230–41.
[33] Reinhardt HW. Fracture mechanics of an elastic softening material like concrete. Heron; 1984. p. 29.
[34] Simões JT, Ruiz MF, Muttoni A. Validation of the Critical Shear Crack Theory for punching of slabs without transverse reinforcement by means of a refined mechanical model. Struct Concrete 2018;19:191–216.
[35] Taylor HPJ. Investigation of the Forces Carried Across Cracks in Reinforced Concrete Beams in Shear by Interlock of Aggregate. Number 42.447 in Technical report (Cement and Concrete Association). London, United Kingdom; 1970.
[36] Tirassa M, Fernández Ruiz M, Anciaux G, Muttoni A. Interface stresses in cracked concrete: testing for review of its fundamentals. In: 2017 fib symposium high tech concrete: where technology and engineering meet. Maastricht, Netherlands; 2017, pp. 740–748.
[37] Tirassa M, Fernández Ruiz, Miguel, Muttoni A. Modern experimental research techniques for a consistent understanding of aggregate interlocking. In: Proceedings of the 12th fib PhD symposium in civil engineering. Prague, Czech Republic; 2018, pp. 723–730.
[38] Ulaga T. Betonbauteile mit Stab-und Lamellenbewehrung: Verbund-und Zuggliedmodellierung. Ph.D. Thesis ETH Zurich Switzerland; 2003.
[39] Walraven JC. Aggregate interlock: a theoretical and experimental analysis Ph.D Thesis Delft University of Technology Sweden; 1980.
[40] Walraven JC. Fundamental analysis of aggregate interlock. ASCE J Struct Div 1981;107:2245–70.
[41] Walraven JC, Vos E, Reinhardt HW. Experiments on shear transfer in cracks in concrete. Part I. Technical Report Delft University of Technology, Faculty Civil Engineering and Geosciences; 1979.
[42] Wittmann FH. Structure of concrete with respect to crack formation. Fract Mech Concrete 1983;43:6.
[43] Østergaard, Olesen, Poulsen. Biaxial testing machine for mixed mode cracking of concrete. Fracture mechanics of concrete and concrete structures, vol. 1. Catania, Italy: CRC Press; 2007. p. 8.